Neoplasma 2025; 72(4): 262–274

doi:10.4149/neo_2025_250411N162

EGLN2 attenuates ovarian cancer malignancy via ferroptosis activation

Yue WU[1,#], Haiyan CHEN[1,#], Shengyuan JIANG[1], Xiaoli WU[2], Dake LI[1,*], Kaipeng XIE[2,3,*]

[1]*Department of Gynecology, Women's Hospital of Nanjing Medical University, Nanjing Women and Children's Healthcare Hospital, Nanjing, China;* [2]*Department of Women Health Care, Women's Hospital of Nanjing Medical University, Nanjing Women and Children's Healthcare Hospital, Nanjing, China;* [3]*Department of Public Health, Women's Hospital of Nanjing Medical University, Nanjing Women and Children's Healthcare Hospital, Nanjing, China*

**Correspondence: lidake2002@163.com; kaipengxie@njmu.edu.cn*
[#]Contributed equally to this work.

Received April 11, 2025 / Accepted August 4, 2025

Growing evidence indicates that ferroptosis is pivotal in the development and progression of ovarian cancer (OC). However, the function of EGLN2 in OC remains unclear. In this study, we observed that EGLN2 is expressed at low levels in OC tissues and is associated with a favorable prognosis in early-stage patients based on data from TCGA and GTEx public databases. Compared with those in normal ovarian epithelial cell lines, *EGLN2* mRNA and protein levels were significantly lower in OC cell lines. *In vitro* functional experiments revealed that EGLN2 overexpression reduced proliferation, increased the intracellular levels of iron ions, reactive oxygen species, lipid peroxidation, and mitochondrial oxidative phosphorylation, and inhibited the Warburg effect. Mechanistically, EGLN2 inhibited the expression of HIF-1α, which binds to the promoter of ceruloplasmin (CP), reducing the proliferation of and inducing ferroptosis in OC cells. A subcutaneous xenograft model in nude mice demonstrated that EGLN2 overexpression inhibited HIF-1α, promoted ferroptosis, and inhibited OC cell growth. In summary, EGLN2 suppressed CP transcription and increased ferroptosis in OC cells. These findings provide new insights into OC development and open avenues for innovative therapies.

Key words: ovarian cancer; ferroptosis; EGLN2; HIF-1α; ceruloplasmin

Ovarian cancer (OC) remains the most lethal malignancy affecting the reproductive system of females [1]. By the year 2024, 19,680 new cases of OC were anticipated to be diagnosed solely in the United States, and despite notable progress in diagnostic techniques, surgical interventions, and therapeutic modalities, 12,740 women were projected to lose their lives to this disease [2]. The development of OC is a multifactorial, multistep, and complex process [3] that involves the activation of signaling pathways, including RAS [4], VEGF [5], HIF, and NF-κB [6] pathways. Given the complexity of tumorigenesis and tumor progression, a comprehensive understanding of the biological mechanisms underlying the malignant characteristics of OC is crucial for developing effective treatment strategies.

Hypoxia is a defining feature of the tumor microenvironment and significantly contributes to tumorigenesis and treatment resistance; it facilitates the Warburg effect, where enhanced glycolytic metabolism creates a local hypoxic environment that supports cancer cell proliferation [7]. Concurrently, this hypoxic milieu enables tumor cells to evade cell death through various mechanisms [8]. Egl-9 family hypoxia inducible factor 2 (*EGLN2*), also known as prolyl hydroxylase domain 1 (*PHD1*) [9], requires molecular oxygen as a substrate for hydroxylation and relies on α-ketoglutarate (α-KG) and Fe^{2+} as cofactors to catalyze the hydroxylation of hypoxia-inducible factor (*HIF*) [10]. Notably, *EGLN2* has been recognized as a driver gene of ferroptosis from FerrDb V2 (http://www.zhounan.org/ferrdb/) [11] and plays a role in regulating the occurrence of iron death in cancer cells [12]. Ferroptosis plays a critical role in suppressing tumorigenesis by eliminating cells that are nutrient-deficient or damaged [13]. Iron metabolism within cells includes iron absorption, utilization, storage, and export [14]. Imbalances in iron homeostasis are central to ferroptosis in tumor cells [15]. Circulating Fe^{3+} is imported into cells via transferrin receptors (TFRCs), reduced to Fe^{2+}, and then used by the cells, where it is stored as ferritin (including *FTH1*) or exported via ferroportin (*FPN1*). Excess Fe^{2+} can undergo the Fenton reaction [16], generating reactive oxygen species (ROS) that peroxidize membrane lipids, leading to

cell death [17, 18]. Erastin leads to the accumulation of lipid ROS and ultimately results in ferroptosis by inhibiting system Xc- (a cystine–glutamate antiporter) activity, cystine uptake, and downstream glutathione (GSH) synthesis [19, 20]. Growing evidence indicates that ferroptosis involves multiple signaling pathways, including an imbalance in iron homeostasis [21], alterations in oxidative stress and hypoxia-related transcription factors [22], lipid peroxidation [23], and cystine uptake and transport [24]. The glutathione peroxidase (GPX) family, particularly GPX4, mediates lipid peroxidation. The cystine/glutamate transporter (system Xc-) facilitates cystine uptake. Moreover, accumulating evidence suggests that targeting the process of ferroptosis could be a promising strategy for treating OC [25].

Different roles of *EGLN2* have been described in various types of cancers. For example, *EGLN2* inhibits angiogenesis in lung cancer [26], and *EGLN2* overexpression promotes the proliferation of breast cancer cells [27]. Under hypoxic conditions, *EGLN2* promotes chemoresistance in bladder cancer by inhibiting *HIF-1α* degradation [28]. In human fibrosarcoma cells, *EGLN2* induces ferroptosis by degrading *HIF-1α*, which prevents ferroptosis by increasing fatty acid uptake and lipid storage [29]. Moreover, *HIF-1α* promotes cervical cancer invasion and migration [30]. As a transcription factor, *HIF-1α* regulates more than 100 downstream genes involved in tumor proliferation [31], metastasis [32], ferroptosis [33], glycolysis [34], lipid metabolism [35], and angiogenesis [36]. However, the function of *EGLN2* in OC remains unexplored. The roles of the *EGLN2*/*HIF-1α* axis in regulating ferroptosis have not been fully elucidated. Therefore, we investigated the effects and underlying mechanisms of *EGLN2* on the malignant phenotype of OC and ferroptosis of OC cells.

Materials and methods

Cell lines and cell culture. The human OC cell lines SKOV3, A2780, and OVCAR3, as well as the normal human ovarian epithelial cell lines IOSE386 and IOSE80, were procured from Procell Life Science & Technology Co., Ltd. (Wuhan, China). A2780, IOSE386, and IOSE80 cells were grown in high-glucose DMEM (KeyGEN, China) supplemented with 10% fetal bovine serum (Gibco, USA). OVCAR3 cells were cultured in RPMI-1640 medium (KeyGEN, China), and SKOV3 cells were cultured in McCoy's 5A medium (KeyGEN, China). All cells were grown in a humidified incubator at 37 °C with 5% CO_2. The normal human ovarian epithelial cell lines IOSE386 and IOSE80 were kindly provided by Dr. Xu Juan (Women's Hospital of Nanjing Medical University, China).

ROS assay. The cellular ROS level was assessed using a reactive oxygen species detection kit (Beyotime, China). 2',7'-dichlorodihydrofluorescein diacetate (DCFH-DA) was diluted to a concentration of 10 μmol/l in serum-free medium. After the cell culture medium was removed, 1 ml of diluted DCFH-DA was added to each well of a 6-well plate. The cells were subsequently incubated at 37 °C for 30 min. Then, the cells were washed with DMEM three times and then digested with 0.25% trypsin. The cells were washed twice with PBS and resuspended in 300 μl of PBS. The fluorescence intensity of DCFH-DA was detected by flow cytometry. The cells were subsequently washed with DMEM three times and cultured with serum-free DMEM. The absorbance (Ex: 488 nm, Em: 525 nm) was determined with a microplate reader (Bio-Tek, USA).

Malondialdehyde (MDA) assay. MDA levels were measured using a lipid peroxidation assay kit (Dojindo, Japan). Briefly, cells were seeded in 10 cm cell culture dishes at 5×10^6 cells/well for 24 h. Then, the MDA detection solution was added to cell lysates, which were then heated in a 95 °C boiling water bath for 15 min, cooled in an ice bath for 5 min, and then centrifuged at 10,000 × g for 10 min. The absorbance (Ex: 540 nm, Em: 590 nm) was determined with a microplate reader (Bio-Tek, USA).

Iron assay. The relative Fe^{2+} level in cell lysates was measured with an Iron Assay Kit (Abcam). The Fe^{2+} in cell lysates was reacted with Ferene-S for 30 min at 37 °C, producing a stable-colored complex. The absorbance (593 nm) was analyzed with a microplate reader (Bio-Tek, USA). In addition, the cells were cultured to the desired density and then sequentially incubated with 1 μg/ml Hoechst solution and 1 μmol/l FerroOrange solution at 37 °C for 30 min. Following incubation, the cells were examined using a confocal fluorescence microscope.

GSH assay. Cells were seeded in 6 cm cell culture dishes. A reduced GSH assay kit (Jian Cheng Technology, China) was then used when the cells reached an appropriate density. The optical density (OD) value was measured at 405 nm using a microplate reader and normalized to the number of cells in each group.

The Seahorse assay. Metabolic indicators (oxygen consumption rate (OCR) and extracellular acidification rate (ECAR)) were usually used to evaluate glycolytic flux. Treated OC cells were added to an XF24 cell culture plate at a density of 5×10^4 cells/well. After rehydration, the probe was incubated with cells overnight in an incubator at 37 °C without CO_2. To perform the OCR assay, the cells were incubated for 1 h in basal analytical medium supplemented with 2 mM glutamine, 10 mM glucose, and 1 mM pyruvate before analysis with an XF Cell Mito Stress Kit (Seahorse Bioscience, USA). The working concentrations of oligomycin, FCCP, and rotenone were 1.5 μM, 1.5 μM, and 0.5 μM, respectively. For the ECAR assay, the cells were incubated for 1 h with 2 mM glutamine and 1 mM pyruvate before analysis with a glycolysis test kit (Seahorse Bioscience, USA). The working concentrations of glucose, oligomycin, and 2-deoxyglucose (2-DG) were 10 mM, 1.5 μM, and 50 mM, respectively.

Targeted metabolomics analysis. To analyze central carbon metabolites, targeted metabolomic analyses were conducted using human OC cells (n=3/group) via HPIC-MS/MS. Metabolomic analysis was performed using a Dionex

ICS-6000 HPIC System (Thermo Scientific, USA) coupled with a QTRAPTM 6500 triple quadrupole mass spectrometer (AB SCIEX, USA). A total of 56 analytes were identified via MRM with the electrospray ionization source in negative mode. The final dataset containing information on the compound name, sample name, and concentration was imported into SIMCA 16.0.2 software (Sartorius Stedim Data Analytics AB, Umea, Sweden) for multivariate analysis.

Subcutaneous xenograft model in nude mice. All procedures involving animals were approved by the Ethics Committee of The Affiliated Obstetrics and Gynecology Hospital of Nanjing Medical University (No. 2023KY034) and followed international ethical guidelines for animal research. Twelve female BALB/c nude mice (4–6 weeks old) were divided equally into two groups after one week of acclimatization. SKOV3 cells (1×10^7 cells) overexpressing *EGLN2* lentivirus or control lentivirus were separately inoculated into the left axilla of each mouse. We measured and recorded the tumor size and weight of each mouse every 4–5 days. The mice were euthanized 30 days after subcutaneous tumor injection, and the tumor tissues were harvested and weighed, and the tumor volume was measured. Tumor tissues were immediately fixed in paraformaldehyde or frozen in liquid nitrogen for subsequent processing.

Lentivirus and plasmid transfection. Plasmid constructs and vector lentivirus were purchased from Genechem (Shanghai, China). We established indicated gene (*EGLN2*) overexpression cell lines. Briefly, the two types of OC cells were inoculated into 6-well plates. The following day, according to multiplicity of infection (MOI) and viral titer, we needed to add the appropriate amount of virus into complete medium, calculated by the formula: viral volume = (MOI × number of cells) / viral titer. Cells were cultured in cell culture medium containing 2 μg/ml puromycin (Beyotime, China) once they reached 90% confluence. Every other day, the cell culture medium was replaced with fresh medium containing 2 μg/ml puromycin until a stable cell line with high overexpression efficiency was achieved.

Bioinformatics analysis. Statistical analysis and visualization of data from The Cancer Genome Atlas (TCGA) or the Genotype-Tissue Expression (GTEx) databases were performed using the GEPIA2 (Gene Expression Profiling Interactive Analysis, http://gepia2.cancer-pku.cn/), which was employed to analyze gene expression in OC. The KM plotter (Kaplan-Meier plotter, http://kmplot.com) database evaluates the survival of EGLN2 in different stages of OC.

Cell proliferation. Cell proliferation was detected by the cell count kit-8 (CCK-8, Dojindo, Japan), 5-ethynyl-2'-deoxyuridine (EdU), and colony formation assays. To perform the CCK-8 assay, cells were seeded into 96-well plates (SKOV3: 3,000 cells/well, OVCAR3: 6,000 cells/well) with three replicates per sample. After 0, 24, 48, and 72 h, cell culture media with CCK-8 reagent at a mixed ratio of 1:10 was added (100 μl/well). After 1.5 h of incubation, cell proliferation was estimated through a microplate reader (Bio-Tek, USA) at a wavelength of 450 nm. Colony formation assays cultivated cells for 2 weeks after seeding 1,000 of them into 6-well plates. After 20 min of fixation in 4% paraformaldehyde, the cells were stained for 20 min in 0.1% crystal violet (Beyotime, China). For the EdU assay, cells were inoculated into 96-well plates at 2×10^4 cells/well. After 24 h, cells were cultured for 2 h with EdU-working solution. Subsequent fixation and staining were performed according to the EdU (RiboBio, China) instructions and photographed using the fluorescent microscope.

Western blotting (WB) analysis. The collected cells were lysed with a mixture of protein lysate and protease inhibitor cocktail (RIPA:cocktail = 100:1). Protein concentration was adjusted to 2 μg/μl by the Bicinchoninic acid assay. Protein samples (15 μg each) were separated on a 10% Trispolyacryl gel (Invitrogen) by electrophoresis and transferred onto Polyvinylidene Fluoride (PVDF) membranes. The membranes were blocked with 5% skim milk powder for 2 h at room temperature and then were stained at 4 °C overnight with specific primary antibodies (Supplementary Table S1). After incubating with the secondary antibody (horseradish peroxidase-conjugated anti-rabbit IgG [Biosharp, 1:5,000 dilution]) for 2 h at room temperature, the membranes were visualized with an enhanced chemiluminescence (ECL) solution.

RNA extraction and quantitative real-time PCR (qRT-PCR). Total RNA was purified by GeneJET RNA Purification Kit (Thermo, USA) and cDNA reverse transcribed with HiScript III Reverse Transcriptase (Vazyme, China) according to the manufacturer's instructions. qRT-PCR was performed using SYBR Green Mix (Vazyme, China) by the ABI StepOnePlus Real-Time PCR machine (Applied Biosystems, USA). Relative expression of the target genes was calculated using $2^{-\Delta\Delta CT}$ with β-actin as an internal reference. Primers of target genes for qRT-PCR are shown in Supplementary Table S2.

RNA sequencing analysis. SKOV3 cells transfected with the EGLN2 overexpression plasmid or empty vector were directly collected using TRIzol. RNA sequencing was conducted by Shenzhen Huada Gene Science and Technology Service Company. The BGISEQ platform was used for sequencing six samples, yielding an average data output of 1.19 GB per sample. The final results showed an average alignment rate of 93.40% against the genome and 89.30% against the gene set.

Dimethyloxallyl glycine (DMOG) treatment. Cells were treated with 100 μM DMOG (prepared by diluting a 100 mM DMSO stock in complete medium) for 24 hours. Control cells received medium containing 0.1% DMSO. Protein lysates were collected for subsequent analysis.

Immunohistochemistry (IHC). Tissues were fixed for paraffin embedding, and paraffin slicers were utilized to obtain approximately 5 μm-thick sections. The tissue sections designated for staining were deparaffinized in xylene, followed by rehydration in anhydrous ethanol. Subse-

quently, the samples were stained, air-dried, and sealed. IHC was performed according to the instructions provided with the specialized kit. The ImageJ IHC Profiler categorized the intensity of cell staining as follows: negative = 1, weak positive = 2, positive = 3, and high positive = 4 [37]. The percentage of mildly stained cells in each category was determined. The staining intensity score was then multiplied by the percentage of positive cells to yield a final score [38].

Dual-luciferase reporter assays. The JASPAR website (https://jaspar.genereg.net/) was used for online prediction of HIF-1α transcription factor binding sites with CP. The Dual-Luciferase Reporter kit (Yeasen, Shanghai) was used for the detection of the luciferase activities according to the manufacturer's protocol. The wild-type CP promoter was inserted into a pGL3-basic luciferase reporter vector. HEK-293T cells were lysed in 24-well plates for 20 min at room temperature using 200 µl cell lysis buffer. Subsequently, 20 µl of the lysate was mixed with 100 µl of each reagent in a 96-well opaque white enzyme labelling plate. The luciferase activities were detected with a microplate reader (Bio-Tek, USA) within 30 min. The results are expressed as a ratio of firefly to Renilla.

Statistical analysis. The data are presented as means ± standard deviations (SDs). To assess significant differences in the data, statistical analyses were conducted using either one-way ANOVA or two-tailed t tests. Each experiment was conducted independently at least three times (*p<0.05, **p<0.01, ***p<0.001; NS-nonsignificant; #p<0.05, ##p<0.01, and ###p<0.001).

Results

***EGLN2* is expressed at low levels in OC and indicates a favorable prognosis in the early stage.** We first compared the mRNA levels of the *EGLN2* gene in human OC samples using data from the TCGA and GTEx public databases. Our study revealed that *EGLN2* mRNA levels were notably lower in OC tissues than in normal tissues (p<0.05) (Figure 1A). The expression of *EGLN2* was notably lower in advanced OC tissues (stages III and IV) than in stage II OC tissues

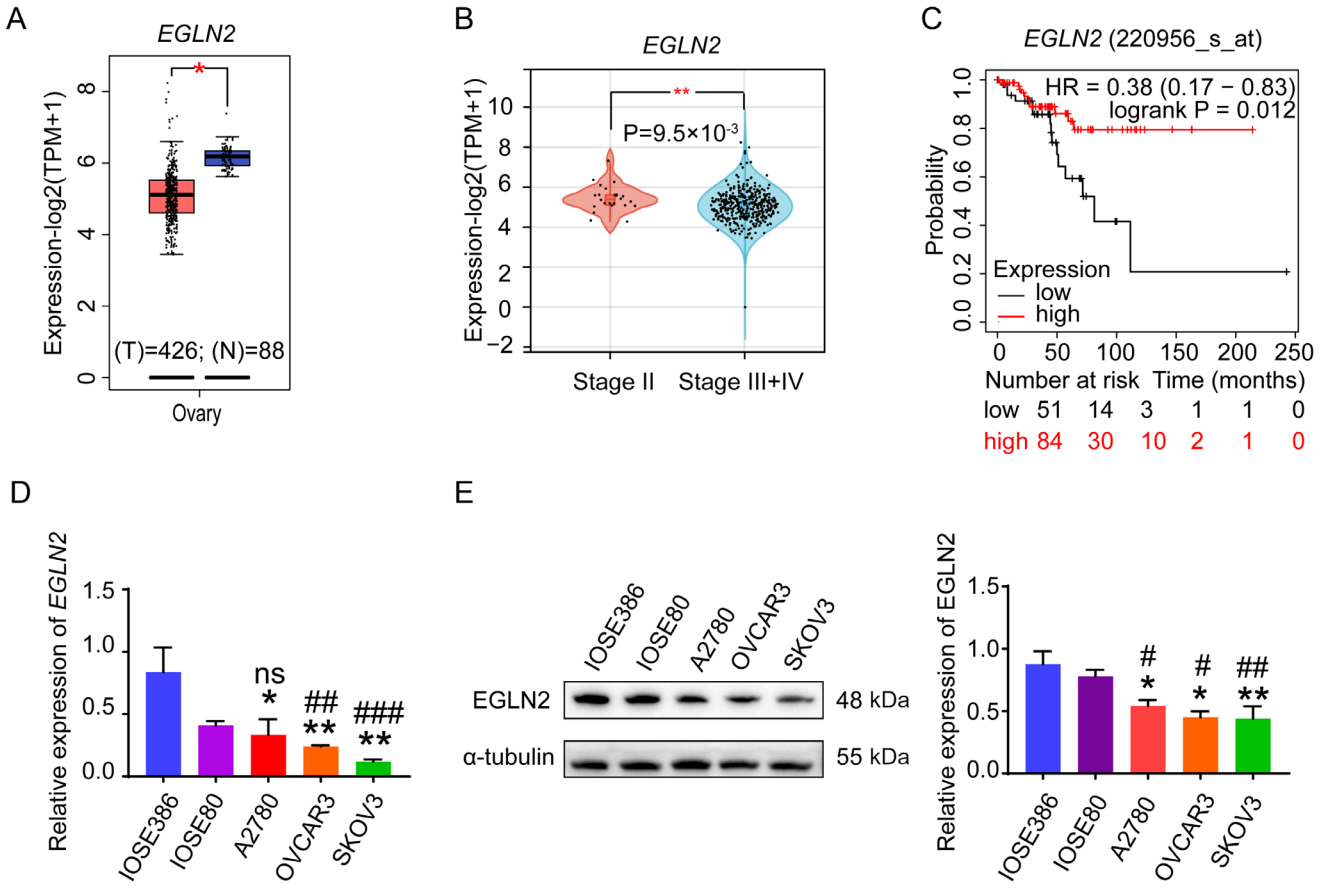

Figure 1. Expression of *EGLN2* in OC and its correlation with FIGO stage and survival. A) Comparison of *EGLN2* mRNA expression levels between normal ovarian tissues and OC tissues in the TCGA and GTEx databases. B) Assessment of *EGLN2* mRNA expression across OC tissues at various FIGO stages. C) Analysis of the correlation between *EGLN2* expression and OS in early-stage OC patients (stages I and II) using the KM Plotter website. D, E) *EGLN2* mRNA and protein expression levels in normal ovarian epithelial cell lines and epithelial OC cell lines (IOSE386: *; IOSE80: #).

(Figure 1B). Kaplan-Meier survival analysis revealed significantly better overall survival (OS) in early-stage OC patients (stages I and II) with high *EGLN2* expression than in those with low *EGLN2* expression (p=0.012) (Figure 1C). Additionally, the expression levels of *EGLN2* were lower at the mRNA and protein levels in human OC cell lines (A2780, OVCAR3, and SKOV3) than in normal ovarian epithelial cells (IOSE386 and IOSE80), as indicated by WB and qRT-PCR (Figures 1D, 1E).

***EGLN2* overexpression significantly inhibits the proliferation of OC cells *in vitro*.** On the basis of the above comparisons of mRNA and protein expression in cell lines, we subsequently overexpressed *EGLN2* in the SKOV3 and OVCAR3 cell lines. WB analysis confirmed that *EGLN2* protein levels were significantly elevated in the *EGLN2*-overexpressing groups (Figure 2A). Furthermore, the growth rate of the *EGLN2*-overexpressing cells was significantly lower than that of the control cells (Figure 2B). Additionally, the results of the EdU incorporation and colony formation assays further demonstrated that elevated *EGLN2* expression significantly inhibited the proliferation of OC cells (Figures 2C, 2D).

***EGLN2* is closely associated with ferroptosis.** We performed RNA sequencing analysis, which revealed that the overexpression of *EGLN2* in SKOV3 cells resulted in 111 genes being upregulated and 220 genes being downregulated compared with those in the control group (|fold change (FC)| >1.5, Q value <0.05) (Figure 3A). KEGG analysis revealed that the genes with differential expression were associ-

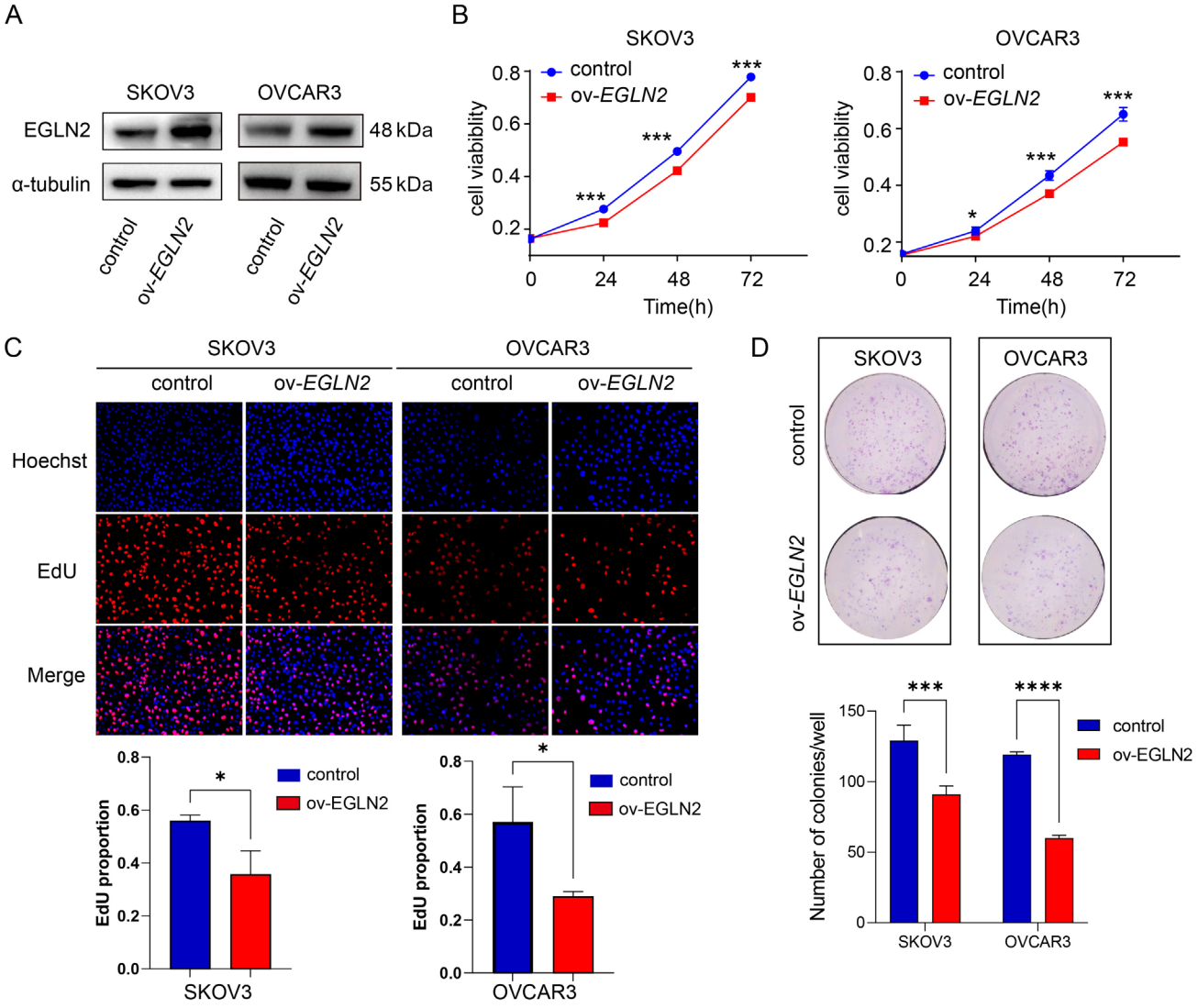

Figure 2. *EGLN2* overexpression inhibits OC cell proliferation. A) Comparison of EGLN2 protein expression in control and *EGLN2*-overexpressing SKOV3 and OVCAR3 cells. B) Cell viability was analyzed using the CCK-8 assay. C) Cell proliferation was assessed by the EdU assay. Cell nuclei were stained with Hoechst 33342 (blue). Scale bar = 200 μm. D) Representative images of colony formation assays conducted using control and *EGLN2*-overexpressing SKOV3 and OVCAR3 cells.

ated with ferroptosis, hypoxia, and amino acid biosynthesis (Figure 3B). Moreover, the molecular function (MF) module from the Gene Ontology (GO) analysis indicated that the differentially expressed genes were related to functions such as metal ion binding, ATP binding, and transferase activity (Figure 3C). Furthermore, gene set enrichment analysis (GSEA) revealed that genes in the *EGLN2* overexpression group were significantly enriched in the oxidative phosphorylation pathway (Figure 3D).

***EGLN2* overexpression increases the intracellular levels of iron ions, ROS, and lipid peroxidation.** Our findings indicated that the overexpression of *EGLN2* resulted in a decrease in the IC50 value of erastin in SKOV3 cells, suggesting that *EGLN2* overexpression synergistically enhances erastin-induced ferroptosis in OC cells (Figure 4A). The total intracellular iron content increased by approximately 40% in the *EGLN2* overexpression group, predominantly in the form of Fe^{2+} (Figure 4B). Subsequent treatment with erastin prompted ferroptosis in the cells; however, measurements using the FerroOrange fluorescent probe revealed that Fe^{2+} levels remained significantly elevated in the *EGLN2*-overexpressing group (Figure 4C). Iron uptake is mediated by the binding of transferrin to *TFRC*. Following the acidification of endosomes and the release of iron from transferrin, Fe^{2+} can be utilized, stored as *FTH1*, or exported from the cell via *FPN1*. The protein expression of *TFRC* and *FPN1* was significantly reduced in the *EGLN2*-overexpressing group, whereas that of *FTH1* was significantly increased (Figure 4D). These data suggest that excessive intracellular iron accumulation following *EGLN2* overexpression may contribute to cell death.

Our results demonstrated that ROS accumulation was significantly greater in the *EGLN2*-overexpressing group than in the control group (Supplementary Figures S1A, S1B). Lipid peroxidation serves as a crucial indicator of ferroptosis, with both lipid ROS and MDA being byproducts of lipid peroxidation and recognized as markers for this process. We observed that lipid peroxidation levels were markedly elevated in the *EGLN2*-overexpressing group relative to those in the control group (Supplementary Figures S1C, S1D), whereas GSH levels were significantly reduced in the *EGLN2*-overexpressing group (Supplementary Figure S1E). Additionally, we noted that the expression levels of *HO-1*, *SLC7A11*, and *GPX4* were decreased in the *EGLN2*-overexpressing group (Supplementary Figure S1F). On the basis of these findings, we propose that *EGLN2* can synergize with erastin to promote ferroptosis in OC cells.

***EGLN2* overexpression promotes mitochondrial OXPHOS and inhibits the Warburg effect.** Elevated levels of ROS and the accumulation of Fe^{2+} promote ferroptosis in cells [39]. Changes in mitochondrial morphology are consid-

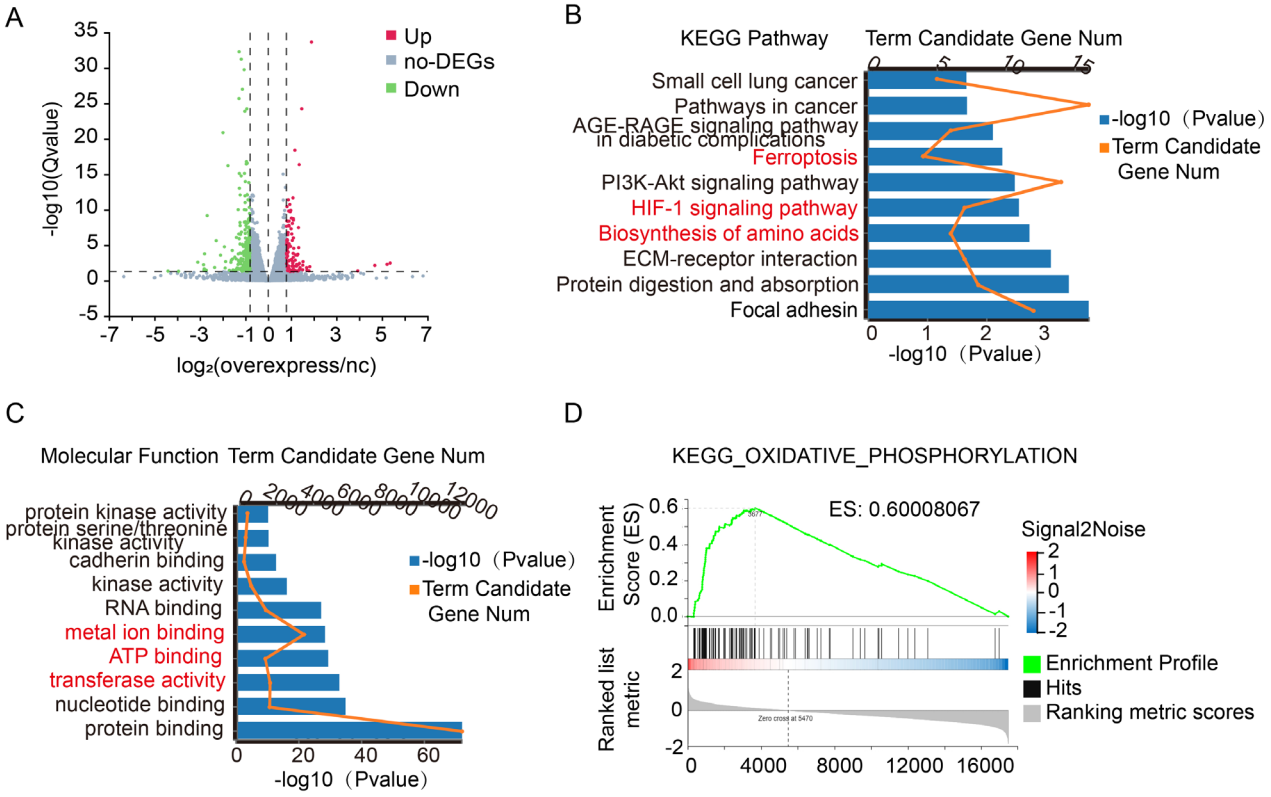

Figure 3. ***EGLN2* is closely associated with ferroptosis. A) Volcano plots illustrating differential gene expression in control and *EGLN2*-overexpressing SKOV3 cells (no-DEGs: non-differentially expressed genes). B) KEGG pathway analysis highlighting the top 10 most significantly associated pathways. C) GO analysis of the top 10 most significantly associated molecular functions. D) Representative GSEA results demonstrating enrichment patterns.**

ered hallmarks of ferroptosis [40]. Transmission electron microscopy revealed that SKOV3 cells overexpressing *EGLN2* presented an increase in the number and a decrease in the size of mitochondria, along with increased membrane density and a reduction in cristae (Figure 5A). Given that mitochondrial OXPHOS is the primary source of intracellular ROS [41], these mitochondrial changes also occurred in OVCAR3 cells (Figure 5B). As illustrated, the *EGLN2*-overexpressing group presented increased basal respiration (BR), maximal respiration (MR), spare respiratory capacity (SRC), proton leakage (PL), and ATP-linked respiration (AP), as well as increased nonmitochondrial oxygen consumption (NMOC) (Figure 5C). The increase in NMOC aligns with the increased activity of α-ketoglutarate-dependent dioxygenases (α-KGDDs) [42]. A heatmap of the differentially expressed mitochondria-related genes obtained from RNA sequencing highlighted *SPARC*, *NTSR1*, *ANKRD37*, *P4HA1*, and *MUC1* as the five genes whose expression was most significantly altered (Figure 5D). In our study of OVCAR3 cells, we observed a decrease in glycolysis in the *EGLN2*-overexpressing group (Figure 5E). Notably, in both SKOV3- and OVCAR3 overexpressing *EGLN2* cells, we observed a significant reduction in *HK2* [43] and *LDHA* [44] expression (Supplementary Figure S2), two key glycolytic enzymes that establish HIF-1α transcriptional targets and central mediators of the Warburg effect in cancer [45].

***EGLN2* overexpression increases central carbon metabolites.** We analyzed central carbon metabolites by HPIC-MS/MS in both the OVCAR3 cell line overexpressing *EGLN2* and the control. On the basis of the PCA results, a difference between the two groups of samples was evident, as all samples fell within the 95% confidence interval (Supplementary Figure S3A). For each comparison set, we calculated Euclidean distance matrices on the basis of the quantitative values of the metabolites. We then clustered the metabolites using a fully chained approach and presented the results in a heatmap (Supplementary Figure S3B). The analysis of 56 central carbon metabolism-related metabolites revealed that eight metabolites were significantly increased in the *EGLN2*-overexpressing group. Among these, the five most prominent were ribose 5-phosphate, adenosine diphosphate, guanosine diphosphate, citric acid, and glucaric acid. The results of the boxplot analysis revealed that several of these metabolites may be involved in glycolysis, the pentose phosphate pathway

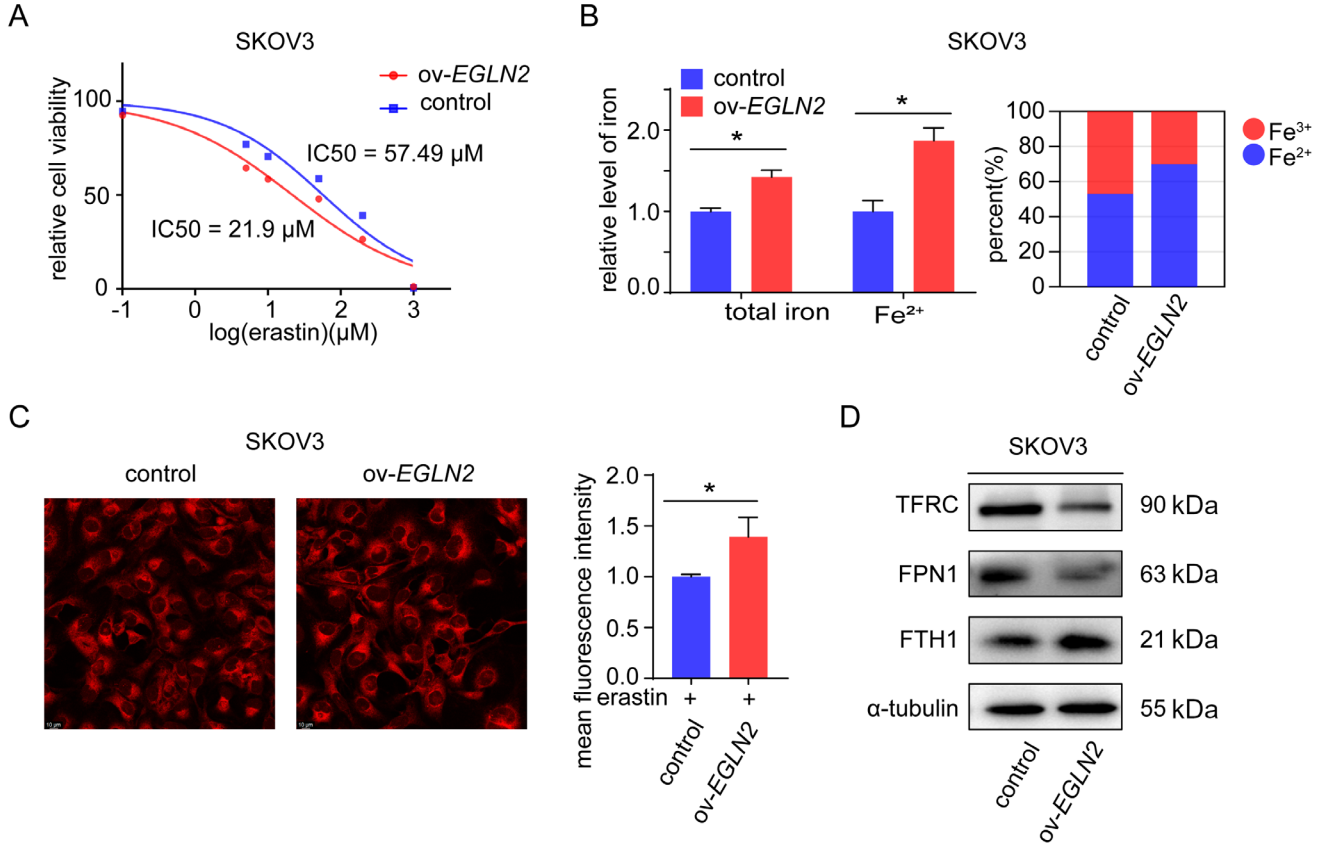

Figure 4. Disturbed iron metabolism in *EGLN2*-overexpressing cells. A) Changes in the IC50 values of erastin in cells overexpressing *EGLN2*. B) Total iron and ferrous ion levels (left) and the ratio of Fe^{2+} to Fe^{3+}among intracellular iron ions (right) in *EGLN2*-overexpressing cells assessed using a ferric iron assay kit. C) Representative images depicting Fe^{2+} colocalization in *EGLN2*-overexpressing cells following incubation with erastin (20 μM) for 12 h. Scale bar = 10 μm. D) Protein expression levels of *TFRC*, *FPN1*, and *FTH1* in *EGLN2*-overexpressing cells.

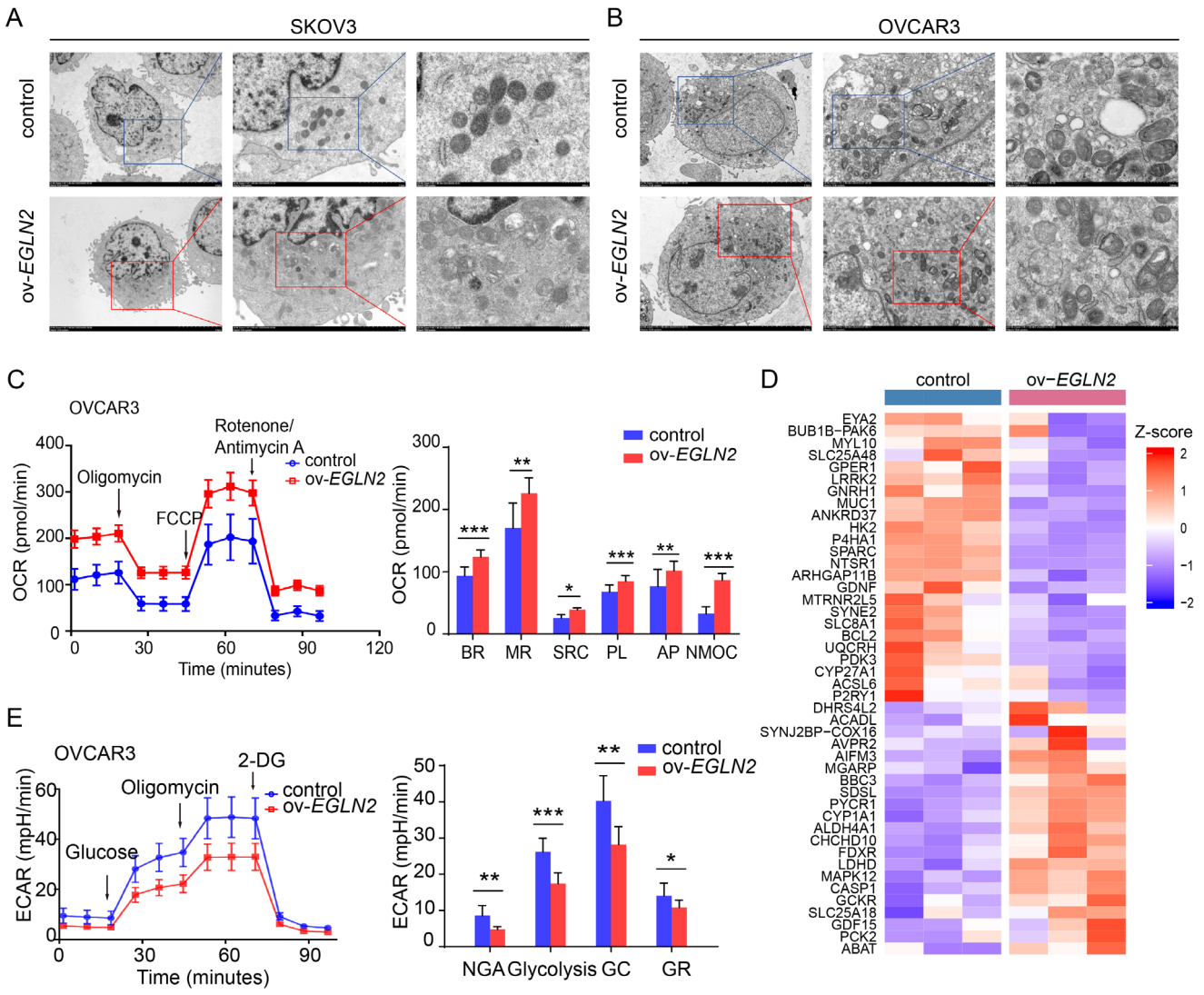

Figure 5. Altered mitochondrial number, morphology, biological function, and glycolytic flux in *EGLN2*-overexpressing cells. A) Representative transmission electron microscopy images of SKOV3-overexpressing *EGLN2* cells and control cells. Scale bars: 5 μm (left), 2.0 μm (middle), and 0.5 μm (right). B) Representative transmission electron microscopy images of OVCAR3 cells overexpressing *EGLN2* and control cells. Scale bars: 5 μm (left), 1.0 μm (middle), and 0.5 μm (right). C) Enhancement of the OCR, including BR, MR, SRC, PL, AP, and NMOC, in the *EGLN2*-overexpressing group. D) Heatmap of differentially expressed mitochondria-associated genes (z-score normalized). E) Decreased ECAR, including nonglycolytic acidification (NGA), glycolytic capacity (GC), and glycolytic reserve (GR) in the *EGLN2*-overexpressing group.

(PPP), and the tricarboxylic acid cycle (TCA) (Supplementary Figure S3C).

***EGLN2* mediates *HIF-1α* downregulation and inhibits CP transcription to promote ferroptosis.** Given that *EGLN2* can inhibit *HIF-1α* activation [46], we first investigated the relationship between *EGLN2* and *HIF-1α* in OC. Our findings indicated that the overexpression of *EGLN2* led to a decrease in *HIF-1α* expression. In addition, DMOG is well known as a hypoxia mimetic agent. Notably, even under hypoxic conditions, *HIF-1α* protein levels were significantly reduced (Supplementary Figure S4A). The RNA sequencing results revealed that *EGLN2* overexpression did not impact HIF-1α mRNA expression levels. To explore the effect of the EGLN2/HIF-1α axis on ferroptosis in OC, we focused on CP, which was identified as the most downregulated gene associated with ferroptosis in the RNA-seq data (log2 ratio = –1.18, Q value = 1.63×10^{-15}). The database indicated that CP mRNA levels were elevated in OC (Supplementary Figure S4B). Furthermore, we observed that CP protein expression was decreased in the *EGLN2*-overexpressing group (Supplementary Figure S4C). HIF-1α is known to promote *CP* transcription [47]. To elucidate the relationship between these two factors, we analyzed the binding profiles of HIF-1α to the CP promoter region using the JASPAR database. The results

indicated that HIF-1α binds to the CP promoter region (Supplementary Figure S4D). Moreover, the overexpression of HIF-1α in SKOV3 cells resulted in increased mRNA levels of *CP* and protein levels of CP, TFRC, and FPN1 (Supplementary Figures S4E, S4F). HIF-1α was shown to bind to the wild-type CP promoter (Supplementary Figure S4G).

***CP* overexpression rescues the inhibitory effects of *EGLN2* overexpression on tumor proliferation and the promotion of ferroptosis.** The overexpression efficiency of the CP protein in SKOV3 and OVCAR3 cells infected with control lentiviral particles, as well as in SKOV3 and OVCAR3 cells overexpressing *CP* following *EGLN2* overexpression, was evaluated through WB (Figure 6A). Compared with control cells, OC cell lines that overexpressed *CP* following the overexpression of *EGLN2* presented a noteworthy increase in growth rate, as determined by the CCK-8 assay (Figures 6B, 6C). EdU experiments further confirmed that the overexpression of *CP* reversed the tumor growth inhibition caused by the overexpression of *EGLN2* (Figure 6D). After the cells were exposed to erastin for 12 hours to induce cell death, analysis with the FerroOrange fluorescent probe indicated a significant decrease in Fe^{2+} levels compared with the previous levels in the cells overexpressing *CP* (Figure 6E). We observed that the expression levels of *TFRC*, *FPN1* and *FLC* were significantly elevated in the *CP*-overexpressing group following *EGLN2* overexpression, whereas the changes in *FTH1* expression were not pronounced (Supplementary Figure S5).

***EGLN2* inhibits OC progression and promotes ferroptosis *in vivo*.** We employed an *in vivo* nude mouse subcutaneous xenograft tumor model. Thirty days after tumor cell injection, we examined gross specimens and photographed the dissected subcutaneous tumors. Compared with that in the control group, the tumor size in the *EGLN2*-overexpressing group was significantly smaller (Supplementary Figure S6A), and the tumor weight was notably lower (Supplementary Figure S6B). Under microscopic observation, both groups exhibited large, loosely arranged tumor cells with large, deeply stained nuclei and common mitotic figures, which were consistent with the histological characteristics

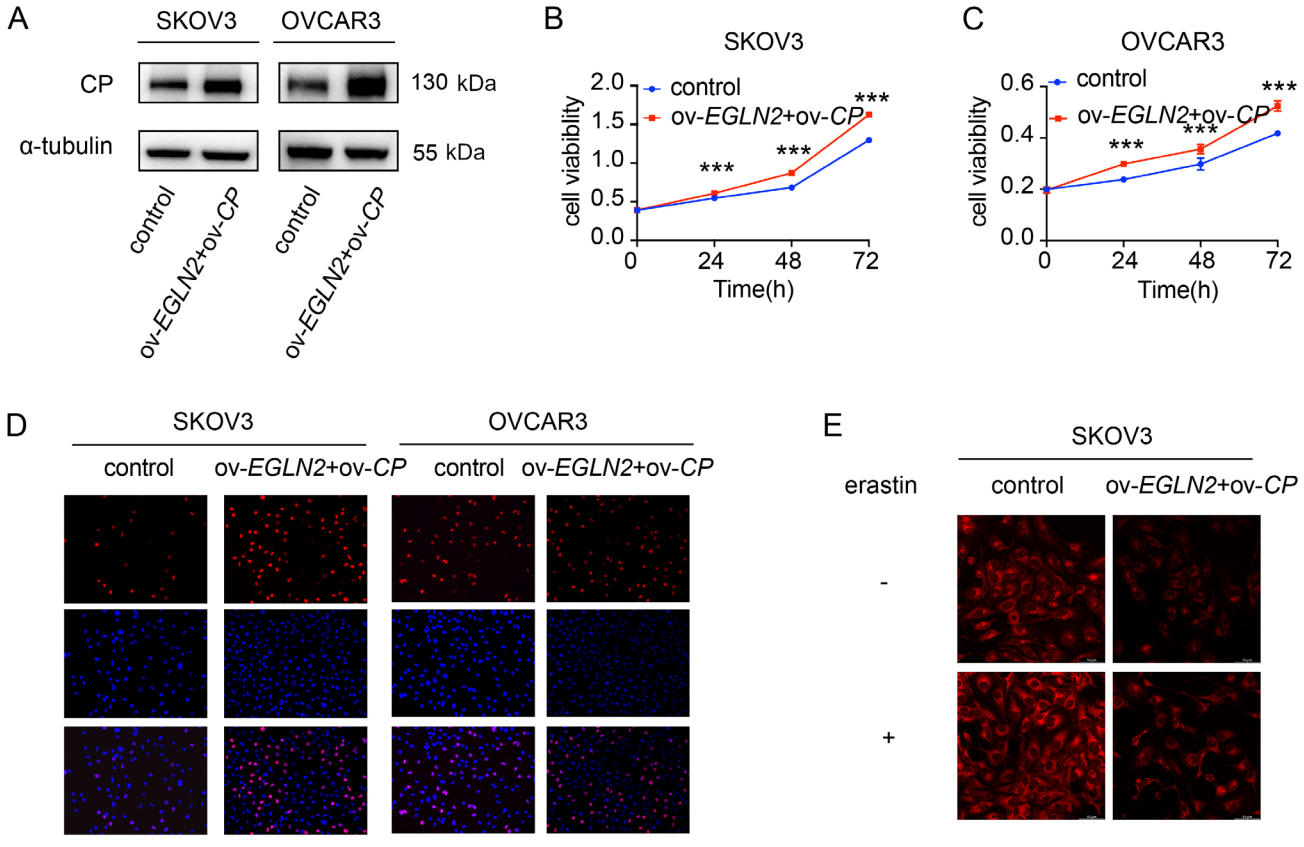

Figure 6. *CP* overexpression can rescue the effects caused by *EGLN2* overexpression. A) Efficiency of *CP* protein overexpression in SKOV3 and OVCAR3 cells infected with control lentiviral particles, as well as after the overexpression of *CP* following *EGLN2* overexpression. B, C) Growth curves depicting the proliferation of SKOV3 and OVCAR3 cells overexpressing *CP* subsequent to *EGLN2* overexpression. D) EdU assays were performed to assess the overexpression of *CP* following *EGLN2* overexpression in SKOV3 and OVCAR3 cells (scale bar = 200×). E) Representative confocal images of Fe^{2+} levels in SKOV3 cells overexpressing *CP* subsequent to *EGLN2* overexpression following 12 h of incubation with erastin. Scale bar = 10 μm.

of the tumor cells and confirmed the successful establishment of the xenograft model (Supplementary Figure S6C). In the *EGLN2*-overexpressing group, the expression levels of nuclear proliferation markers, such as *PCNA* and *Ki-67*, were significantly reduced (Supplementary Figure S6C). Additionally, the protein expression of *HIF-1α* and *CP*, which we focused on, followed a similar trend to that observed *in vitro*, with decreased levels due to *EGLN2* overexpression (Supplementary Figure S6D). The immunohistochemical scores for these proteins were significantly different between the groups (Supplementary Figure S6E). Moreover, an analysis of OC tissues from 12 nude mice revealed an inverse correlation between *HIF-1α* expression and *EGLN2* expression, as well as a positive correlation with *CP* expression (Supplementary Figure S6F). Notably, we also observed elevated iron levels in the tumors of the *EGLN2*-overexpressing group (Supplementary Figure S6G).

Discussion

In this study, we investigated *EGLN2* as a key factor in OC and its connection to ferroptosis. First, the results revealed that *EGLN2* expression was significantly downregulated in both OC tissues and cell lines. *In vitro* functional experiments revealed that the overexpression of *EGLN2* significantly inhibited the proliferation of OC cells and promoted ferroptosis. The overexpression of *EGLN2* enhanced mitochondrial OXPHOS and impaired glycolysis. This study further demonstrated that the overexpression of *EGLN2* inhibited *CP* via the suppression of *HIF-1α*, promoted ferroptosis, and suppressed the growth of OC cells. Subcutaneous tumor formation in nude mice demonstrated that *EGLN2* overexpression inhibited *HIF-1α*, promoted ferroptosis, and inhibited OC cell growth.

Ferroptosis is characterized by iron ion overload, lipid peroxidation, and the dysregulation of antioxidant defenses [48]. Our study demonstrated that *EGLN2* modulates ferroptosis under normoxic conditions through changes in cellular morphology, functional properties, and genetic alterations. *EGLN2* overexpression in OC cells promoted ferroptosis by increasing the levels of intracellular Fe^{2+}, ROS, and lipid peroxidation markers and decreasing GSH levels. These findings confirmed the critical role of iron homeostasis in regulating ferroptosis. Iron metabolism imbalance is often characterized by increased iron uptake and decreased iron transport and utilization [49, 50]. Interestingly, while *TFRC* expression decreased and *FTH1* expression increased, which is typically indicative of reduced ferroptosis, the exact intracellular mechanisms that might mitigate ferroptosis following *EGLN2* overexpression remain unclear and warrant further investigation.

Moreover, our study revealed elevated levels of intracellular lipid peroxidation, along with decreased *GPX4*, *SLC7A11*, and *HO-1* expression. Electron microscopy in the present study revealed that *EGLN2*-overexpressing cells had smaller mitochondria, denser membranes, and fewer cristae; the Seahorse assay further demonstrated enhanced mitochondrial OXPHOS and decreased glycolysis. Previous studies have indicated that an increase in the number of mitochondria, changes in morphology, and enhanced biological functions (such as OXPHOS) can lead to a reduction in cellular glycolytic flux [51]. Cancer cells are commonly known to prefer aerobic glycolysis over OXPHOS [52]. In addition, the increase in glycolytic flux may be a compensatory mechanism to maintain ATP levels [53].

In our investigation of the molecular changes and regulatory mechanisms by which *EGLN2* influences cellular ferroptosis, we referred to previous literature suggesting that the EGLN family functions as a proline hydroxylase of *HIF-1α* under normoxic conditions. *HIF-1α* is known to be a crucial factor involved in regulating cellular ferroptosis. Our experiments revealed decreased HIF-1α protein expression in cells overexpressing *EGLN2*, which aligns with the observed increase in the mitochondrial OCR in these cells. In our study, we confirmed that the imbalance in iron homeostasis was a central focus. On the basis of the RNA-seq results, we postulated that *CP* is downstream of the *EGLN2*/*HIF-1α* axis. We observed that the transcript and protein levels of *CP* significantly increased after *HIF-1α* overexpression. Using the JASPAR database, we identified the most likely binding site between *HIF-1α* and *CP* (ATACGTTA), with a correlation score of 0.91. It is known that *HIF-1α* promotes *CP* transcription. Accumulating evidence has demonstrated that HIF-1α-mediated glycolytic reprogramming promotes ovarian cancer progression and confers resistance to chemotherapy, as established in prior studies [54–56]. In the future, we will further validate whether *HIF-1α* can promote *CP* transcription through a chromatin immunoprecipitation (ChIP) assay and verify whether *HIF-1α* can target the promoter region of *CP* through the predicted binding site.

In vivo findings indicated that increased *EGLN2* expression hindered OC progression through ferroptosis-mediated cell death. Notably, changes in the expression levels of *TFRC*, *FTH1*, *FPN1*, and *CP* during ferroptosis are subject to ongoing debate. *CP*, a copper-containing glycoprotein and a member of the multicopper oxidase family [57], is known for its role in inhibiting Fe^{2+}-mediated ROS production and protecting against oxidative stress [58]. CP is crucial for oxidizing iron ions, converting Fe^{2+} to Fe^{3+}, and facilitating the binding of Fe^{3+} to transferrin [59]. CP and FPN1 work together to export cellular iron into the bloodstream and regulate intracellular Fe^{2+} levels [60]. In our study, the increased intracellular Fe^{2+} levels observed in *EGLN2*-overexpressing cells were associated with the decreased expression of *CP* and *FPN1*, leading to a reduction in iron efflux and an increase in intracellular iron stores, which contributed to an imbalance in iron homeostasis. This research sheds new light on the mechanisms underlying OC development and identifies potential pathways for innovative treatment strategies.

In conclusion, *EGLN2*, a tumor suppressor gene, is associated with cancer stage. High *EGLN2* expression is correlated with improved prognosis in early-stage OC. *EGLN2* overexpression in OC promotes ferroptosis by increasing the levels of intracellular Fe^{2+}, ROS, and lipid peroxidation markers and decreasing GSH levels. Moreover, *EGLN2* overexpression increases mitochondrial oxidative phosphorylation, suppresses the Warburg effect, downregulates *HIF-1α* expression, inhibits *CP* transcription, and facilitates ferroptosis.

Supplementary information is available in the online version of the paper.

Acknowledgments: This study was supported by grants from the Natural Science Foundation of Jiangsu Province (BK20221183), Jiangsu Province Association of Maternal and Child Health Foundation (FYX202344), and Nanjing Medical Science and Technique Development Foundation (YKK23156).

References

[1] KARIA PS, JOSHU CE, VISVANATHAN K. Uptake and Predictors of Opportunistic Salpingectomy for Ovarian Cancer Risk Reduction in the United States. Cancer Prev Res (Phila) 2021; 14: 1101–1110. https://doi.org/10.1158/1940-6207.CAPR-21-0121

[2] SIEGEL RL, GIAQUINTO AN, JEMAL A. Cancer statistics, 2024. CA Cancer J Clin 2024; 74: 12–49. https://doi.org/10.3322/caac.21820

[3] BATTAGLIA AM, SACCO A, VECCHIO E, SCICCHITANO S, PETRIAGGI L et al. Iron affects the sphere-forming ability of ovarian cancer cells in non-adherent culture conditions. Front Cell Dev Biol 2023; 11: 1272667. https://doi.org/10.3389/fcell.2023.1272667

[4] THERACHIYIL L, ANAND A, AZMI A, BHAT A, KORASHY HM et al. Role of RAS signaling in ovarian cancer. F1000Res 2022; 11: 1253. https://doi.org/10.12688/f1000research.126337.1

[5] Bizzaro F, Fuso Nerini I, Taylor MA, Anastasia A, Russo M et al. VEGF pathway inhibition potentiates PARP inhibitor efficacy in ovarian cancer independent of BRCA status. J Hematol Oncol 2021; 14: 186. https://doi.org/10.1186/s13045-021-01196-x

[6] YU X, WANG Y, QIU H, SONG H, FENG D et al. AEG-1 Contributes to Metastasis in Hypoxia-Related Ovarian Cancer by Modulating the HIF-1alpha/NF-kappaB/VEGF Pathway. Biomed Res Int 2018; 2018: 3145689. https://doi.org/10.1155/2018/3145689

[7] VAUPEL P, SCHMIDBERGER H, MAYER A. The Warburg effect: essential part of metabolic reprogramming and central contributor to cancer progression. Int J Radiat Biol 2019; 95: 912–919. https://doi.org/10.1080/09553002.2019.1589653

[8] SEMENZA GL. Hypoxia-inducible factors in physiology and medicine. Cell 2012; 148: 399–408. https://doi.org/10.1016/j.cell.2012.01.021

[9] KAELIN WG JR, RATCLIFFE PJ. Oxygen sensing by metazoans: the central role of the HIF hydroxylase pathway. Mol Cell 2008; 30: 393–402. https://doi.org/10.1016/j.molcel.2008.04.009

[10] FANDREY J, GORR TA, GASSMANN M. Regulating cellular oxygen sensing by hydroxylation. Cardiovasc Res 2006; 71: 642–651. https://doi.org/10.1016/j.cardiores.2006.05.005

[11] ZHOU N, YUAN X, DU Q, ZHANG Z, SHI X et al. FerrDb V2: update of the manually curated database of ferroptosis regulators and ferroptosis-disease associations. Nucleic Acids Res 2023; 51: D571–D582. https://doi.org/10.1093/nar/gkac935

[12] DAI C, CHEN X, LI J, COMISH P, KANG R et al. Transcription factors in ferroptotic cell death. Cancer Gene Ther 2020; 27: 645–656. https://doi.org/10.1038/s41417-020-0170-2

[13] MOU Y, WANG J, WU J, HE D, ZHANG C et al. Ferroptosis, a new form of cell death: opportunities and challenges in cancer. J Hematol Oncol 2019; 12: 34. https://doi.org/10.1186/s13045-019-0720-y

[14] ZHANG J, CHEN X. p53 tumor suppressor and iron homeostasis. FEBS J 2019; 286: 620–629. https://doi.org/10.1111/febs.14638

[15] BATTAGLIA AM, SACCO A, PERROTTA ID, FANIELLO MC, SCALISE M et al. Iron Administration Overcomes Resistance to Erastin-Mediated Ferroptosis in Ovarian Cancer Cells. Front Oncol 2022; 12: 868351. https://doi.org/10.3389/fonc.2022.868351

[16] MONTESSUIT C, THORBURN A. Activation of Ras by phorbol esters in cardiac myocytes. Role of guanine nucleotide exchange factors. FEBS Lett 1999; 460: 57–60. https://doi.org/10.1016/s0014-5793(99)01223-5

[17] HUANG L, LI W, LU Y, JU Q, OUYANG M. Iron metabolism in colorectal cancer. Front Oncol 2023; 13: 1098501. https://doi.org/10.3389/fonc.2023.1098501

[18] SALATINO A, AVERSA I, BATTAGLIA AM, SACCO A, DI VITO A et al. H-Ferritin Affects Cisplatin-Induced Cytotoxicity in Ovarian Cancer Cells through the Modulation of ROS. Oxid Med Cell Longev 2019; 2019: 3461251. https://doi.org/10.1155/2019/3461251

[19] DIXON SJ, LEMBERG KM, LAMPRECHT MR, SKOUTA R, ZAITSEV EM et al. Ferroptosis: an iron-dependent form of nonapoptotic cell death. Cell 2012; 149: 1060–1072. https://doi.org/10.1016/j.cell.2012.03.042

[20] FRIEDMANN ANGELI JP, KRYSKO DV, CONRAD M. Ferroptosis at the crossroads of cancer-acquired drug resistance and immune evasion. Nat Rev Cancer 2019; 19: 405–414. https://doi.org/10.1038/s41568-019-0149-1

[21] HASSANNIA B, VANDENABEELE P, VANDEN BERGHE T. Targeting Ferroptosis to Iron Out Cancer. Cancer Cell 2019; 35: 830–849. https://doi.org/10.1016/j.ccell.2019.04.002

[22] FEI Z, LIJUAN Y, JING Z, XI Y, YUEFEN P et al. Molecular characteristics associated with ferroptosis in hepatocellular carcinoma progression. Hum Cell 2021; 34: 177–186. https://doi.org/10.1007/s13577-020-00431-w

[23] MIAO Y, CHEN Y, XUE F, LIU K, ZHU B et al. Contribution of ferroptosis and GPX4's dual functions to osteoarthritis progression. EBioMedicine 2022; 76: 103847. https://doi.org/10.1016/j.ebiom.2022.103847

[24] BADGLEY MA, KREMER DM, MAURER HC, DELGIORNO KE, LEE HJ et al. Cysteine depletion induces pancreatic tumor ferroptosis in mice. Science 2020; 368: 85–89. https://doi.org/10.1126/science.aaw9872

[25] LIANG C, ZHANG X, YANG M, DONG X. Recent Progress in Ferroptosis Inducers for Cancer Therapy. Adv Mater 2019; 31: e1904197. https://doi.org/10.1002/adma.201904197

[26] TSAI YM, WU KL, CHANG YY, CHANG WA, HUANG YC et al. Loss of miR-145-5p Causes Ceruloplasmin Interference with PHD-Iron Axis and HIF-2alpha Stabilization in Lung Adenocarcinoma-Mediated Angiogenesis. Int J Mol Sci 2020; 21. https://doi.org/10.3390/ijms21145081

[27] SETH P, KROP I, PORTER D, POLYAK K. Novel estrogen and tamoxifen induced genes identified by SAGE (Serial Analysis of Gene Expression). Oncogene 2002; 21: 836–843. https://doi.org/10.1038/sj.onc.1205113

[28] QING L, LI Q, YANG Y, XU W, WANG Y et al. Hypoxia-mediated attenuation of EGLN2 inhibition of the NF-kappaB signaling pathway leads to the formation of a loop between HIF-1alpha and MUC1-C promoting chemoresistance in bladder cancer. Mol Carcinog 2024; 63: 1303–1318. https://doi.org/10.1002/mc.23725

[29] YANG M, CHEN P, LIU J, ZHU S, KROEMER G et al. Clockophagy is a novel selective autophagy process favoring ferroptosis. Sci Adv 2019; 5: eaaw2238. https://doi.org/10.1126/sciadv.aaw2238

[30] LI Z, WEI R, YAO S, MENG F, KONG L. HIF-1A as a prognostic biomarker related to invasion, migration and immunosuppression of cervical cancer. Heliyon 2024; 10: e24664. https://doi.org/10.1016/j.heliyon.2024.e24664

[31] ZHANG S, XU H, LI W, JI J, JIN Q et al. MDM2 promotes cancer cell survival through regulating the expression of HIF-1alpha and pVHL in retinoblastoma. Pathol Oncol Res 2023; 29: 1610801. https://doi.org/10.3389/pore.2023.1610801

[32] DANG Y, HUA W, ZHANG X, SUN H, ZHANG Y et al. Anti-angiogenic effect of exo-LncRNA TUG1 in myocardial infarction and modulation by remote ischemic conditioning. Basic Res Cardiol 2023; 118: 1. https://doi.org/10.1007/s00395-022-00975-y

[33] JIANG Y, MAO C, YANG R, YAN B, SHI Y et al. EGLN1/c-Myc Induced Lymphoid-Specific Helicase Inhibits Ferroptosis through Lipid Metabolic Gene Expression Changes. Theranostics 2017; 7: 3293–3305. https://doi.org/10.7150/thno.19988

[34] SHIGETA K, HASEGAWA M, HISHIKI T, NAITO Y, BABA Y et al. IDH2 stabilizes HIF-1alpha-induced metabolic reprogramming and promotes chemoresistance in urothelial cancer. EMBO J 2023; 42: e110620. https://doi.org/10.15252/embj.2022110620

[35] YAMAGUCHI A, MUKAI Y, SAKUMA T, NARUMI K, FURUGEN A et al. Monocarboxylate transporter 4 involves in energy metabolism and drug sensitivity in hypoxia. Sci Rep 2023; 13: 1501. https://doi.org/10.1038/s41598-023-28558-4

[36] PANG L, DUNTERMAN M, XUAN W, GONZALEZ A, LIN Y et al. Circadian regulator CLOCK promotes tumor angiogenesis in glioblastoma. Cell Rep 2023; 42: 112127. https://doi.org/10.1016/j.celrep.2023.112127

[37] TEJEDA ME, CANTO P, TENORIO-TORRES A, OROZCO-ARGUELLES L, CORAL-VÁZQUEZ RM et al. Increased FNDC5/IRISIN protein expression in breast cancer tissue is associated with obesity in postmenopausal women. J Clin Pathol 2021: jclinpath-2020-207249. https://doi.org/10.1136/jclinpath-2020-207249

[38] MENG M, GUO Y, CHEN Y, LI X, ZHANG B et al. Cancer/testis-45A1 promotes cervical cancer cell tumorigenesis and drug resistance by activating oncogenic SRC and downstream signaling pathways. Cell Oncol (Dordr) 2024; 47: 657–676. https://doi.org/10.1007/s13402-023-00891-w

[39] WU H, WANG F, TA N, ZHANG T, GAO W. The Multifaceted Regulation of Mitochondria in Ferroptosis. Life (Basel) 2021; 11. https://doi.org/10.3390/life11030222

[40] XU X, LI Y, WU Y, WANG M, LU Y et al. Increased ATF2 expression predicts poor prognosis and inhibits sorafenib-induced ferroptosis in gastric cancer. Redox Biol 2023; 59: 102564. https://doi.org/10.1016/j.redox.2022.102564

[41] XU S, LI S, BJORKLUND M, XU S. Mitochondrial fragmentation and ROS signaling in wound response and repair. Cell Regen 2022; 11: 38. https://doi.org/10.1186/s13619-022-00141-8

[42] BANH RS, IORIO C, MARCOTTE R, XU Y, COJOCARI D et al. PTP1B controls non-mitochondrial oxygen consumption by regulating RNF213 to promote tumour survival during hypoxia. Nat Cell Biol 2016; 18: 803–813. https://doi.org/10.1038/ncb3376

[43] WANG J, SHAO F, YANG Y, WANG W, YANG X et al. A non-metabolic function of hexokinase 2 in small cell lung cancer: promotes cancer cell stemness by increasing USP11-mediated CD133 stability. Cancer Commun (Lond) 2022; 42: 1008–1027. https://doi.org/10.1002/cac2.12351

[44] SHARMA D, SINGH M, RANI R. Role of LDH in tumor glycolysis: Regulation of LDHA by small molecules for cancer therapeutics. Semin Cancer Biol 2022; 87: 184–195. https://doi.org/10.1016/j.semcancer.2022.11.007

[45] KOCH A, EBERT EV, SEITZ T, DIETRICH P, BERNEBURG M et al. Characterization of glycolysis-related gene expression in malignant melanoma. Pathol Res Pract 2020; 216: 152752. https://doi.org/10.1016/j.prp.2019.152752

[46] APPELHOFF RJ, TIAN YM, RAVAL RR, TURLEY H, HARRIS AL et al. Differential function of the prolyl hydroxylases PHD1, PHD2, and PHD3 in the regulation of hypoxia-inducible factor. J Biol Chem 2004; 279: 38458–38465. https://doi.org/10.1074/jbc.M406026200

[47] MARTIN F, LINDEN T, KATSCHINSKI DM, OEHME F, FLAMME I et al. Copper-dependent activation of hypoxia-inducible factor (HIF)-1: implications for ceruloplasmin regulation. Blood 2005; 105: 4613–4619. https://doi.org/10.1182/blood-2004-10-3980

[48] ZHAO H, XU Y, SHANG H. Ferroptosis: A New Promising Target for Ovarian Cancer Therapy. Int J Med Sci 2022; 19: 1847–1855. https://doi.org/10.7150/ijms.76480

[49] JOKILEHTO T, JAAKKOLA PM. The role of HIF prolyl hydroxylases in tumour growth. J Cell Mol Med 2010; 14: 758–770. https://doi.org/10.1111/j.1582-4934.2010.01030.x

[50] BATTAGLIA AM, SACCO A, GIORGIO E, PETRIAGGI L, ELZANOWSKA J et al. Expulsion of iron-rich ferritin via CD63-mediated exosome drives ferroptosis resistance in ovarian cancer cells. Front Cell Dev Biol 2025; 13: 1532097. https://doi.org/10.3389/fcell.2025.1532097

[51] QUAEGEBEUR A, SEGURA I, SCHMIEDER R, VERDEGEM D, DECIMO I et al. Deletion or Inhibition of the Oxygen Sensor PHD1 Protects against Ischemic Stroke via Reprogramming of Neuronal Metabolism. Cell Metab 2016; 23: 280–291. https://doi.org/10.1016/j.cmet.2015.12.007

[52] DHARASKAR SP, AMERE SUBBARAO S. The mitochondrial chaperone TRAP-1 regulates the glutamine metabolism in tumor cells. Mitochondrion 2023; 69: 159–170. https://doi.org/10.1016/j.mito.2023.02.011

[53] ARAGONES J, SCHNEIDER M, VAN GEYTE K, FRAISL P, DRESSELAERS T et al. Deficiency or inhibition of oxygen sensor Phd1 induces hypoxia tolerance by reprogramming basal metabolism. Nat Genet 2008; 40: 170–180. https://doi.org/10.1038/ng.2007.62

[54] NAN Y, WU X, LUO Q, CHANG W, ZHAO P et al. OTUB2 silencing promotes ovarian cancer via mitochondrial metabolic reprogramming and can be synthetically targeted by CA9 inhibition. Proc Natl Acad Sci U S A 2024; 121: e2315348121. https://doi.org/10.1073/pnas.2315348121

[55] JIN Y, BIAN S, WANG H, MO J, FEI H et al. CRMP2 derived from cancer associated fibroblasts facilitates progression of ovarian cancer via HIF-1alpha-glycolysis signaling pathway. Cell Death Dis 2022; 13: 675. https://doi.org/10.1038/s41419-022-05129-5

[56] MORI Y, OKIMOTO Y, SAKAI H, KANDA Y, OHATA H et al. Targeting PDGF signaling of cancer-associated fibroblasts blocks feedback activation of HIF-1alpha and tumor progression of clear cell ovarian cancer. Cell Rep Med 2024; 5: 101532. https://doi.org/10.1016/j.xcrm.2024.101532

[57] VASHCHENKO G, MACGILLIVRAY RT. Multi-copper oxidases and human iron metabolism. Nutrients 2013; 5: 2289–2313. https://doi.org/10.3390/nu5072289

[58] BAKHAUTDIN B, GOKSOY BAKHAUTDIN E, FOX PL. Ceruloplasmin has two nearly identical sites that bind myeloperoxidase. Biochem Biophys Res Commun 2014; 453: 722–727. https://doi.org/10.1016/j.bbrc.2014.09.134

[59] CHERUKURI S, TRIPOULAS NA, NURKO S, FOX PL. Anemia and impaired stress-induced erythropoiesis in aceruloplasminemic mice. Blood Cells Mol Dis 2004; 33: 346–355. https://doi.org/10.1016/j.bcmd.2004.07.003

[60] SHANG Y, LUO M, YAO F, WANG S, YUAN Z et al. Ceruloplasmin suppresses ferroptosis by regulating iron homeostasis in hepatocellular carcinoma cells. Cell Signal 2020;72:109633. https://doi.org/10.1016/j.cellsig.2020.109633

https://doi.org/10.4149/neo_2025_250411N162

EGLN2 attenuates ovarian cancer malignancy via ferroptosis activation

Yue WU[1,#], Haiyan CHEN[1,#], Shengyuan JIANG[1], Xiaoli WU[2], Dake LI[1,*], Kaipeng XIE[2,3,*]

Supplementary Information

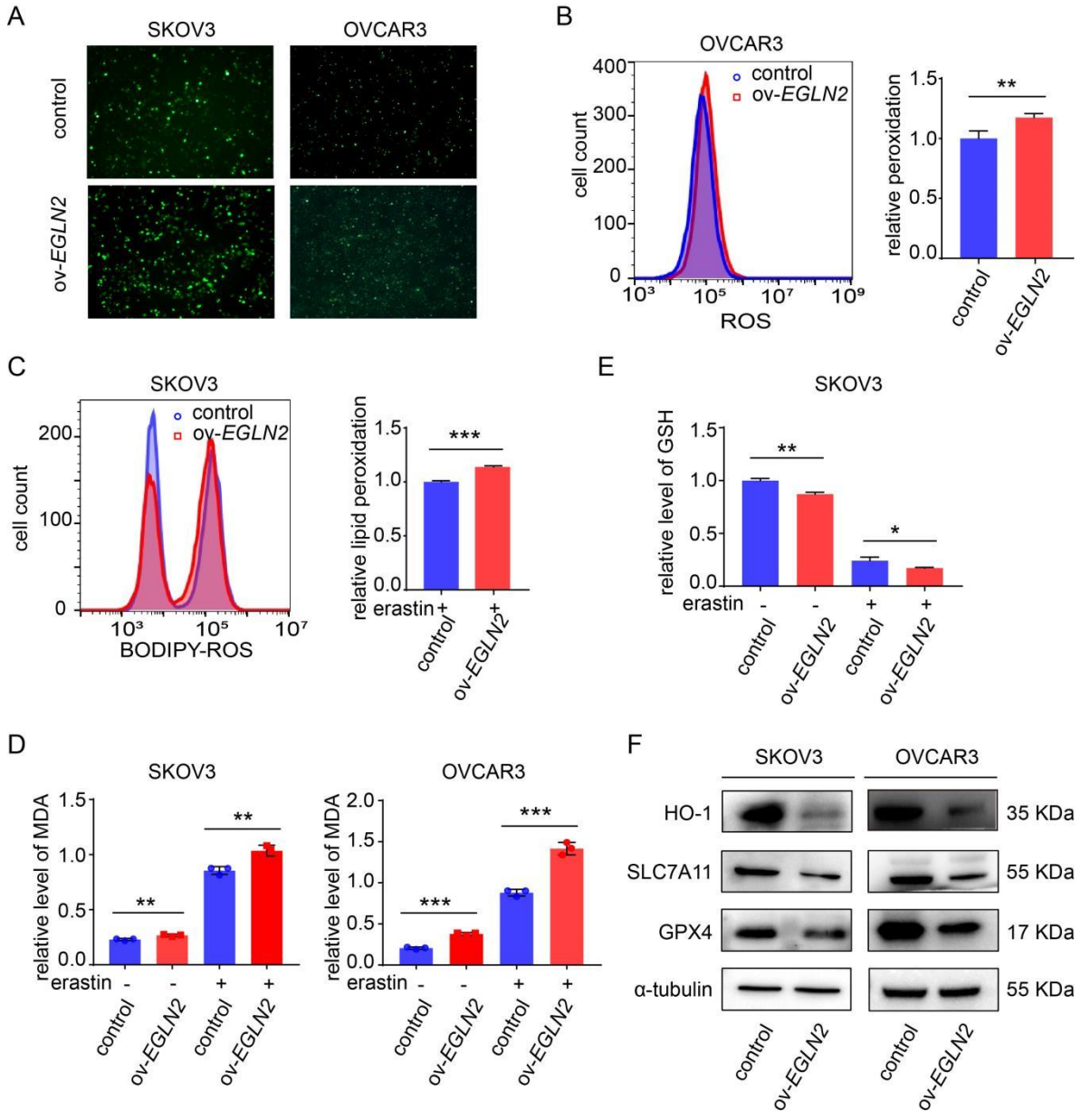

Supplementary Figure S1. Elevated levels of ROS and lipid peroxidation in EGLN2-overexpressing cells. A) Representative images of ROS in EGLN2-overexpressing cells captured via fluorescence microscopy. Scale bar=100 μm. B) Representative flow cytometry images illustrating ROS levels in EGLN2-overexpressing cells. C) Changes in the levels of lipid-related ROS in EGLN2-overexpressing cells following incubation with erastin (20 μM) for 12 h. D) Changes in MDA levels in EGLN2-overexpressing cells. E) Changes in GSH levels in EGLN2-overexpressing cells. F) Changes in the expression levels of HO-1, SLC7A11, and GPX4 in EGLN2-overexpressing cells.

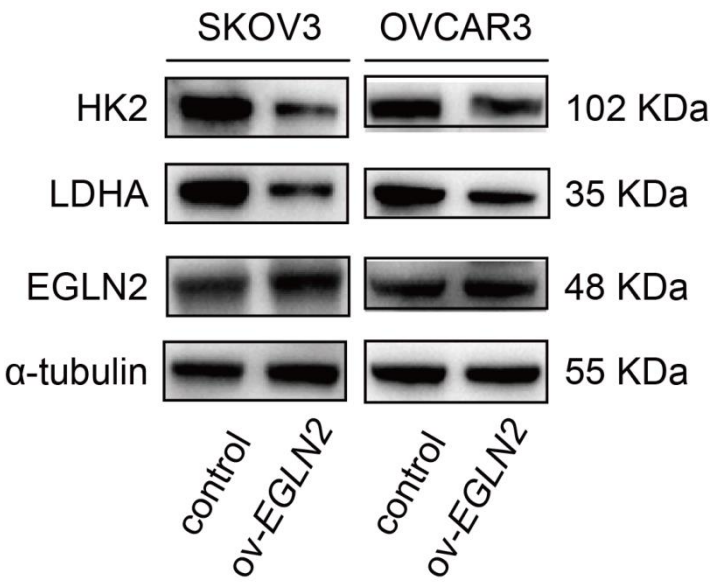

Supplementary Figure S2. Variations in the protein levels of *HK2* and *LDHA* in cells overexpressing *EGLN2*.

Suppl. Table 1. Primary antibodies list.

Antibody	Company	Catalog Number	Molecular weight (kDa)
EGLN2	Proteintech	12984-1-AP	48
α-tubulin	Proteintech	11224-1-AP	55
HO-1	Proteintech	10701-1-AP	35
HK2	Proteintech	22029-1-AP	102
LDHA	Proteintech	21799-1-AP	35
TFRC	ABclonal	A5865	90
FPN1	ABclonal	A14885	63
FTH1	ABclonal	A19544	21
CP	ABclonal	A20229	130
GPX4	ABclonal	A11243	17
SLC7A11	ABclonal	A2413	55
HIF-1α	Cell Signaling Technology	36169	120

Suppl. Table 2. Specific primer sequences for RT-qPCR.

Gene		Primer sequence
EGLN2	Forward	5'-TGGCCCTGGACTATATCGTG -3'
	Reverse	5'-GGCACCAATGCTTCGACAG-3'
CP	Forward	5'-GGGCCATCTACCCTGATAACA-3'
	Reverse	5'-TTAAAGGTCCGATGAGTCCTGA-3'
HIF-1α	Forward	5'-GTGTTATCTGTCGCTTTGAGT-3'
	Reverse	5'-AACTTCACAATCATAACTGGT-3'
β-actin	Forward	5'-TCCCTGGAGAAGAGCTACGA-3'
	Reverse	5'-AGCACTGTGTTGGCGTACAG-3'

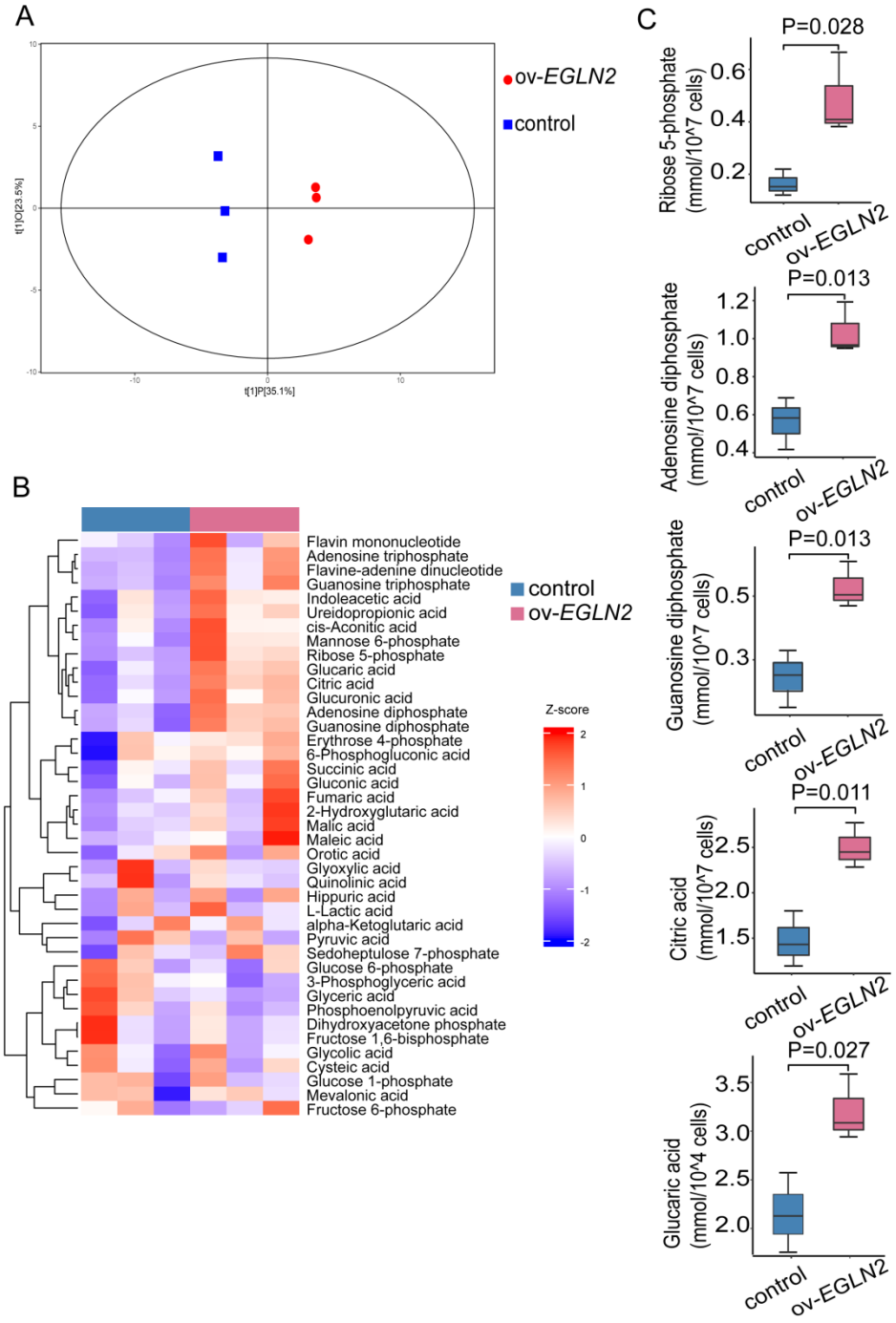

Supplementary Figure S3. Central Carbon Metabolism was assessed in OVCAR3 EGLN2-overexpressing cells and control cells. A) Score scatter plot of the PCA model for OVCAR3 EGLN2-overexpressing cells and control cells. B) Hierarchical clustering of significantly regulated metabolites involved in central carbon metabolism. The color scale indicates relative metabolite levels: red indicates increased metabolites, and blue indicates decreased metabolites. C) Boxplot analysis of five significantly altered metabolites involved in glycolysis, the PPP and the TCA cycle.

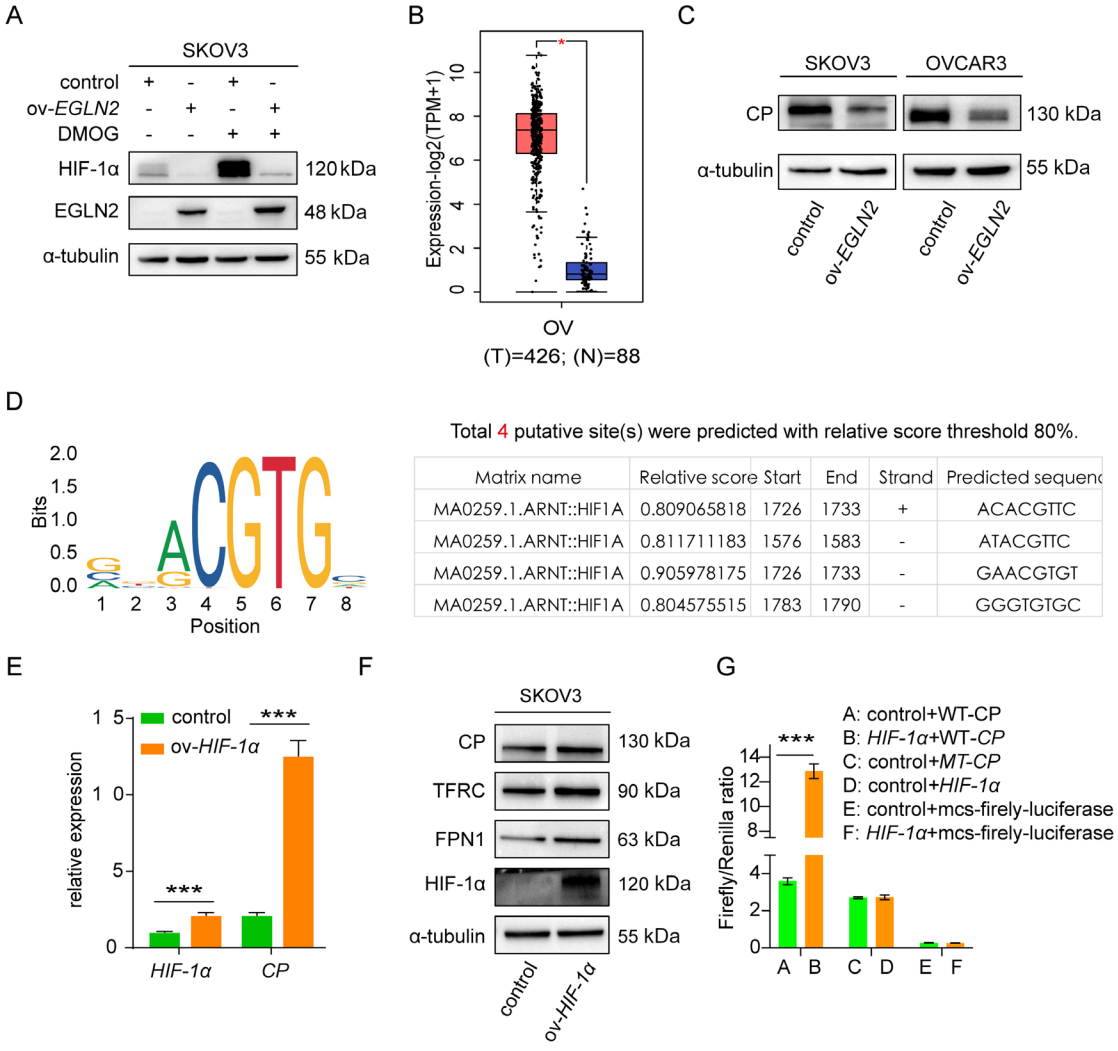

Supplementary Figure S4. *EGLN2* inhibits *CP* transcription to promote ferroptosis by suppressing *HIF-1α* expression. A) HIF-1α expression levels in the EGLN2-overexpressing group under normoxic and hypoxic conditions (100 μM DMOG incubation for 24 h). B) Comparison of CP mRNA expression between normal ovarian tissues and OC tissues on the basis of data from the TCGA and GTEx databases. C) Changes in CP protein expression in the EGLN2-overexpressing group. D) JASPAR database predictions of the binding sites of HIF-1α and the CP promoter. E) Changes in CP mRNA expression levels in the HIF-1α-overexpressing group. F) Changes in the expression levels of CP, TFRC, and FPN1 in HIF-1α-overexpressing cells. G) Dual-luciferase reporter assay demonstrating changes in CP promoter activity in wild-type 293T cells transfected with HIF-1α.

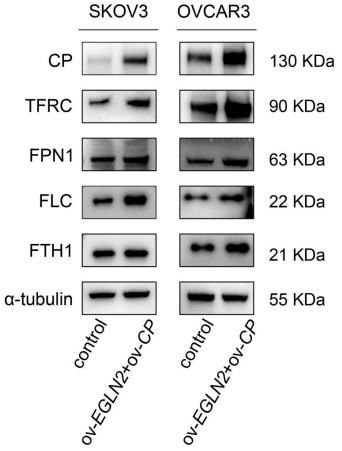

Supplementary Figure S5. Protein expression levels of CP, TFRC, FPN1, FLC, and FTH1 in SKOV3 and OVCAR3 cells overexpressing CP after EGLN2 overexpression.

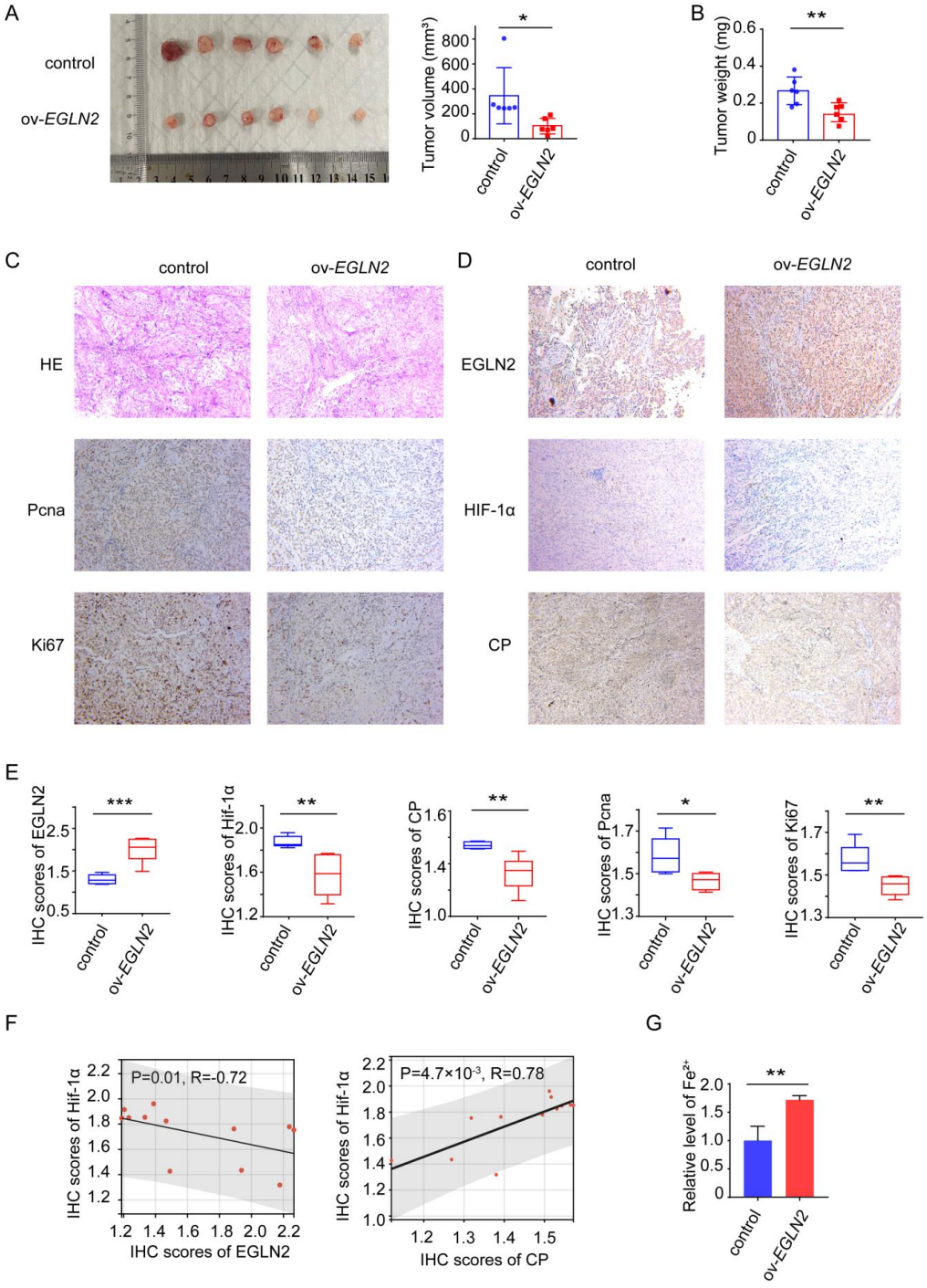

Supplementary Figure S6. Effects of EGLN2 on OC progression and intracellular ferrous ion levels *in vitro*. A) Gross images and volume measurements of subcutaneous tumour growth in two groups of BALB/c female nude mice inoculated with stable EGLN2-overexpressing or control SKOV3 cells. B) Weights of the subcutaneous tumours in the two groups of mice. C, D) Representative images of subcutaneous tumours from mice stained with haematoxylin and eosin (HE) and subjected to immunohistochemical staining (scale bar=40×). E) Statistical analysis of the immunohistochemical scores for PCNA, Ki67, EGLN2, HIF-1α, and CP. F) Relationships between HIF-1α and the expression of EGLN2 and CP. (G) Comparison of ferrous iron content in subcutaneous tumours between the two groups.